Macroinstability Uncovered in a Rushton Turbine Stirred Tank by Means of LES

H. Hartmann, J. J. Derksen, and H. E. A. van den Akker
Kramers Laboratorium voor Fysische Technologie, Delft University of Technology, Prins Bernhardlaan 6, 2628 BW, Delft, The Netherlands

DOI 10.1002/aic.10211
Published online in Wiley InterScience (www.interscience.wiley.com).

Low-frequency mean flow variations, identified experimentally in various stirred-tank geometries, are studied by means of large eddy simulations in a Rushton turbine stirred tank. The focus is on flow structures, and the spectral characteristics of the velocity components. The lattice-Boltzmann Navier-Stokes solver, and the Smagorinsky subgrid-scale model, are adopted for solving the stirred tank flow, and boundary conditions are imposed by means of an adaptive force-field technique. Simulations performed at Reynolds numbers 20,000 and 30,000 on grid sizes of 120^3, 180^3, and 240^3 grid nodes confirm the experimentally found flow variations at various monitoring points in the bulk flow. The period of the flow variations found in the bulk of the tank corresponds to approximately 250 blade passage periods. A simulation performed at a Reynolds number of 12,500 showed pronounced flow variations with a timescale of about 65 blade passage periods, which is consistent with experimental observations. Transient flow field results in the bulk flow of the tank uncover a whirlpool type of precessing vortex, of which the impact on the kinetic energy of the velocity fluctuations is further analyzed. © 2004 American Institute of Chemical Engineers *AIChE J,* 50: 2383–2393, 2004
Keywords: stirred tank, mixing, turbulence, macro-instability, LES

Introduction

Flow phenomena in stirred tanks

Stirred tanks have always played an important role in industry, because of their mixing abilities brought about by the agitation of the impeller together with baffles along the tank wall preventing a solid body rotation of the fluid. As a result, a large number of studies focused on the flow phenomena encountered in such tanks. Rushton et al. (1950) and Holmes et al. (1964) were the among the first to report on power consumption and circulation times for various impeller and tank configurations, which characterize the global flow field. More recently, various experimental and numerical studies reported on local flow information, with a view to optimizing mixing processes (for example, Yianneskis et al., 1987; Schäfer et al., 1998; Derksen et al., 1999; Derksen and Van den Akker, 1999). For instance, the flow structures are identified to be highly three-dimensional (3-D) and complex, with trailing vortices and high-turbulence levels (and dissipation rates) in the vicinity of the impeller. This knowledge of the local flow is of importance as rate-limiting phenomena, such as droplet breakup (Tsouris and Tavlarides, 1994; Luo and Svendsen, 1996) or chemical reactions (Van Vliet et al., 2001) are influenced by the small-scale mixing.

One of the complications in stirred tank flows is the presence of macroinstabilities (MI, that is, low-frequency mean flow variations) that affect the flow patterns and, consequently, mixing performance. Different types of instabilities have been identified experimentally, and were reviewed in the article of Nikiforaki et al. (2002). One of these types was identified as a whirlpool type of vortex moving around the tank centerline (Yianneskis et al., 1987). A large number of studies has been concerned with this instability, and the frequency of its precessing motion at different operating conditions, tank and im-

Correspondence concerning this article should be addressed to H. Hartmann at h.hartmann@klft.tn.tudelft.nl.

peller types, and impeller clearances (for example, Nikiforaki et al., 2002; Haam et al., 1992; Hasal et al., 2000; Myers et al., 1997). However, the frequency was found difficult to reproduce. Nikiforaki et al. (2002) have experimentally pointed out that the whirlpool type of vortex can contribute significantly to the kinetic energy contained in the velocity fluctuations. This effect has similarities to the coherent contribution of the flow periodicity near the impeller blades to the kinetic energy (see for example, Yianneskis et al., 1987; Derksen and Van den Akker, 1999).

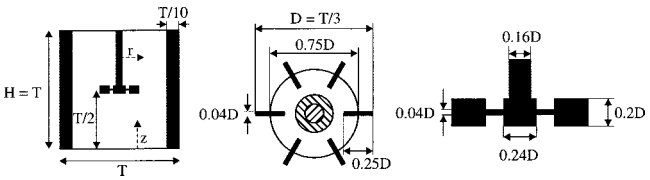

Figure 1. Cross-section of the tank (left). Plan view and cross-section of the impeller (right).

At the top level there is a lid. The impeller, with diameter *D*, is a Rushton turbine.

MI significance to multiphase chemical processes

In chemical processing, the velocity field is used to accomplish objectives such as heat transfer, mass transfer, and chemical reaction. Various investigations provide evidence of the significance of the MI to multiphase chemical processes. Haam et al. (1992) measured the local heat-transfer flux and temperature on the tank wall. Time variations in the local heat-transfer coefficient were observed, and the authors hypothesized that these time variations were due to the precession of an axial vortical structure. Feedstream intermittency was studied by Houcine et al. (1999), by means of laser induced fluorescence (LIF). The feedstream jet was injected at the baffle in the upper part of the tank. Three stages of the feedstream were observed, of which one of them was characterized as effective intermittency with a period of 1-2 s. This phenomenon can be linked to the existence of an MI. Derksen (2003) provided another example of the presence of precessing vortices in a solids distribution system. The lower vortex may contribute to resuspension of the solids lying on the bottom of the tank, and consequently mass transfer is enhanced. However, the voidage in the vortex itself may be regarded as a lost volume. Finally, the upper precessing vortex may cause surface aeration, which often is an unwanted process.

RANS simulation

The presence of low-frequency coherent fluctuations associated with macroinstabilities in stirred tanks have important implications for computational flow models. Commercial software packages generally solve the Reynolds-Averaged Navier-Stokes (RANS) equations in combination with a closure model for the Reynolds stresses. The stationary and rotating components are handled by means of interface models, such as the multiple frames of reference (MFR) technique (CFX-5, 2002). Precessing vortices moving around the tank centerline contribute to the flow unsteadiness, and, therefore, exclude models that allow for a steady-state approximation and domain reduction through geometrical symmetries (for example, frozen-rotor and circumferential-average models). The transient sliding mesh interface, on the contrary, is able to simulate the unsteady fluid motion, as the flow variation both in time and space is taken into account. However, it is unclear what the effect is of the location of the interface between the rotating and stationary meshes on the simulated unsteadiness of the mean flow. Subsequently, the turbulence modeling is a point for discussion. The k-ε model is often used to account for the turbulent fluctuations. This eddy-viscosity model, which locally assumes isotropic turbulent transport, is known to be inappropriate in rotating and/or highly 3-D flows (Wilcox, 1993). Assessment of the isotropy assumptions by LDA experiments (Derksen et al., 1999) and large eddy simulations (Hartmann et al., 2004), has indicated turbulence anisotropy in the impeller stream. Furthermore, in a transient RANS simulation it is not *a priori* clear which part of the fluctuations is temporally resolved, and which part is taken care of by the turbulence model. This especially applies to flows with no clear spectral separation between the low-frequency, coherent fluctuations on one side, and turbulent fluctuations on the other. Experiments in turbulently stirred tanks (for example, Nikiforaki et al., 2002), as well as our LES show no clear separation between MI-related fluctuations, and random fluctuations.

Large eddy simulation

We studied the flow macroinstability numerically by means of large eddy simulation (LES). This methodology is embedded within the lattice-Boltzmann scheme for discretizing the Navier-Stokes equations, and the use of an interface model is avoided by modeling the geometry with an adaptive force field technique (Derksen and Van den Akker, 1999). In LES a clear distinction is made between the resolved and unresolved scales, as the range of resolved scales is limited by the numerical grid. The effect of the unresolved subgrid scales on the resolved large scales is taken into account with a subgrid-scale model. The LES methodology has proven to be a powerful tool to study and visualize stirred tank flows (Eggels, 1996), because it accounts for the unsteady and periodic behavior of these flows, and can effectively be employed to explicitly resolve phenomena directly related to the unsteady boundaries. In terms of velocity fields and kinetic energy, contour plots in the vicinity of the impeller and in the bulk of the tank, assessment of LES proves it to be an accurate method for simulating stirred tank flow (Hartmann et al., 2004). Roussinova et al. (2003) have shown that the circulation pattern instability (that is, another type of macroinstability at a different timescale) can effectively be resolved by means of LES. In this work, the LES methodology will be adopted to identify the whirlpool type of precessing vortex, and its spectral characteristics (for example, characteristic frequency and fluctuation levels).

Flow system

The stirred vessel reactor used in this research was a standard configuration cylindrical vessel of diameter *T*, with four equispaced baffles of width 0.1T, placed at the perimeter of the tank, and with liquid height $H = T$. A lid was positioned at height H. A standard Rushton turbine disk impeller with six blades was mounted at mid-height of the tank. A representation of the geometry is given in Figure 1. Provided that geometric

Table 1. Numerical Setup*

Case	Δ	δt	Re	Res.	Subd.	No. Imp. Revs.	τ
I	$T/120$	$(1200N)^{-1}$	20,000	120^3	4	570	0.69 h
II	$T/180$	$(1600N)^{-1}$	12,500	180^3	6	570	2.03 h
III	$T/180$	$(1600N)^{-1}$	20,000	180^3	6	570	2.03 h
IV	$T/180$	$(1600N)^{-1}$	30,000	180^3	6	570	2.03 h
V	$T/240$	$(2500N)^{-1}$	30,000	240^3	8	150	5.73 h

*The grid spacing Δ and time step δt are given in the first two columns. Subsequently, the Reynolds number, the number of grid nodes and the number of subdomains are given. The number of simulated impeller revolutions times the (wall-clock) time to simulate one impeller revolution, τ, gives the duration of the simulation.

similarity is maintained, the flow system can be fully characterized by the flow Reynolds number, defined as

$$\mathrm{Re} = \frac{ND^2}{\nu} \tag{1}$$

with N the impeller speed, D the impeller diameter, and ν the kinematic viscosity of the working fluid.

Simulation procedure

Large eddy simulation

Many industrially relevant flows are associated with high Reynolds numbers. A direct numerical simulation (DNS) would require enormous amounts of grid cells and time steps, in order to capture all length and timescales present in the flow. In a large eddy simulation (LES), the small scales in the flow are assumed to be universal and isotropic, and the effect the small scales have on the larger scales is modeled with a subgrid-scale model. In this research, the well-known Smagorinsky model (Smagorinsky, 1963) was used. This is an eddy-viscosity model with a subgrid-scale eddy viscosity, ν_e, which is related to the local, resolved deformation rate

$$\nu_e = \lambda_{mix}^2 \sqrt{S^2} \tag{2}$$

where λ_{mix} is the mixing length of the subgrid-scale motion, and S^2 is the resolved deformation rate, defined as

$$S^2 = \frac{1}{2}\left(\frac{\partial u_i}{\partial x_j} + \frac{\partial u_j}{\partial x_i}\right)^2 \tag{3}$$

with u_i the resolved i^{th} velocity component. Note the summation convention over the repeated indices i,j. The ratio between the mixing length, and the lattice spacing Δ is constant, called the Smagorinsky constant (c_s). However, near the walls, the subgrid-scale stresses should vanish, which is not automatically guaranteed in Eq. 2. In general, this is accomplished by a reduction of the length scale λ_{mix} toward the wall. The Van Driest wall damping function (Van Driest, 1956) is applied at the tank walls, which determines the mixing length as

$$\lambda_{mix} = c_s\Delta(1 - e^{-(y^+/A^+)}) \tag{4}$$

where y^+ is the distance to the wall in viscous wall units, and A^+ is a constant taken equal to 26. A value of 0.10 was adopted for c_s, which is a typical value used in LES computations of shear-driven turbulent flows (Piomelli et al., 1988).

A lattice-Boltzmann method (Chen and Doolen, 1998) was used for solving the filtered momentum equations. The specific scheme we used was developed by Somers (1993).

The entire tank was simulated on a uniform, cubic computational grid. Inside the computational domain, the no-slip boundary conditions at the cylindrical tank wall, the baffles, the impeller, and the impeller shaft were imposed by an adaptive force-field technique (Derksen and Van den Akker, 1999).

Simulation aspects

The MI was studied in detail at Re=30,000. Additional simulations have been performed at Re=20,000 and Re=12,500. The size of the computational grid was varied in order to study the influence of the grid-size on the solution. The settings for the simulations are given in Table 1.

The computer code runs on a parallel computer platform by means of domain decomposition: the computational domain was horizontally (that is, perpendicular to the tank centerline) split in a number of equally-sized subdomains.

On every grid node, 21 (18 directions for the LB-particles and 3 force components) single-precision, real values need to be stored. The memory requirements of the simulation are proportional to the grid size, resulting in an executable that occupies in case of the 180^3 grid $180^3 \times 21 \times 4 \approx 0.5$ GByte of memory. The simulations were performed on an in house PC cluster with Athlon 1,800+ MHz processors using an MPI message passing tool for communication within the parallel code.

Within the lattice-Boltzmann framework the time step, and lattice spacing are nondimensional numbers, which are equal to one. Hence, dimensions are expressed in lattice spacings and velocities in lattice units (that is, lattice spacings per time step). In Case I for example, the tank diameter corresponds to 120 lattice spacings, and one impeller rotation corresponds to 1,200 time steps.

During the simulations, the axial, radial, and tangential velocity components were stored on six horizontal lines and four vertical lines. Three horizontal lines were located below the impeller, and three above the impeller. The four vertical lines were located in the impeller outflow stream at different radial positions. The locations of the lines are shown in Figure 2. In case of the 180^3 grid, the radial resolution at the horizontal lines was $0.022T$, with a total number of 23 monitoring points at each line, and the first monitoring point at $2r/T = 0$. The axial resolution at the vertical lines is $0.006T$, with a total number of 25 monitoring points at each line, and the first monitoring point at $z/T = 0.433$. This results in a total number of 238 monitoring points. The sampling frequency f_s equals one

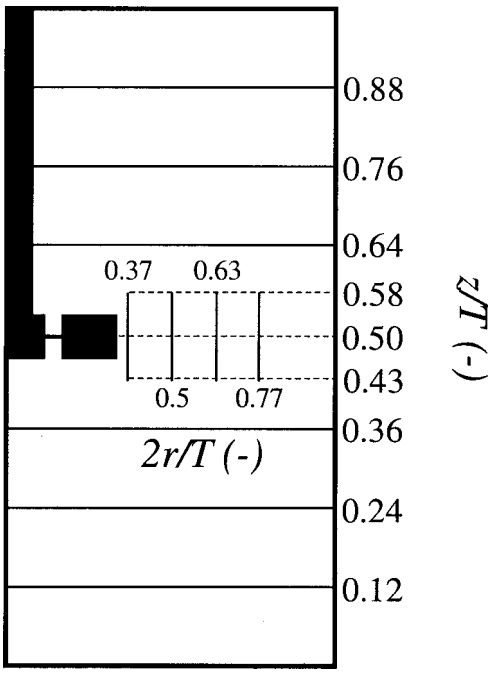

Figure 2. Locations of the horizontal and vertical lines on which the three velocity components are stored.

The vertical plane is located midway between two baffles.

in the lattice Boltzmann framework, as the data are stored at each time step.

The simulations were started from either a zero-velocity field, or from a flow field of a previous simulation. After roughly 20–30 impeller revolutions a quasi steady state was reached. This was checked by monitoring the total kinetic energy as function of time. A flow field was transferred from one grid to the other by means of linear interpolation.

Results

Most of the results presented in this section are based on case IV; Re=30,000. This case serves as a reference case.

Single flow field realizations

The flow field in the vicinity of the tank centerline is shown Figures 3 and 4 at axial positions $z/T = 0.12$ and $z/T = 0.88$, respectively. The contours represent the ratio of the axial vorticity component and the impeller angular speed; a positive value corresponds to fluid rotation in the (clockwise) direction of the impeller rotation. In Figure 3a, the main vortical structure is located in the upper-right corner of the graph. When viewing the graphs in sequence, with a time interval of 11 impeller revolutions between each graph, a precessional motion of the vortex in a clock wise direction (that is, in the same direction as the impeller rotates) around the tank centerline is observed. Note the long period of the precessional motion, being roughly 40–50 impeller revolutions.

Compared to Figure 3, Figure 4a shows a weaker vortical structure in the upper-left corner of the graph. The black circle represents the impeller shaft. Again, the sequence of the graphs shows the vortex precessing around the impeller shaft. A direct comparison between Figures 3 and 4 indicates a phase difference between the upper and lower moving vortices.

Time-series

The transient behavior of the flow strongly depends on the position in the tank. To illustrate the broad range of frequencies encountered in stirred tank flows, the simulated time series of the radial velocity component is depicted in Figure 5 at two typical positions, respectively. At the impeller tip, Figure 5a, most of the fluctuations are periodic as a result of the regular blade passage. This can be clearly seen in the enlarged time series (Figure 5b); the tangential and axial velocity components show a corresponding behavior (not shown). No clear low-frequency oscillations are observed. In the bulk of the tank, Figure 5d, a clear low-frequency, coherent behavior of the radial velocity component is observed. It shows a clear, cyclic variation of the mean flow superimposed on the turbulent fluctuations. The period of the oscillations correspond with the approximated period extracted from the flow field snapshots, around 50 impeller revolutions. This periodic behavior was found less pronounced in the axial velocity component, but the periodicity in the axial velocity component has been observed at various other positions in the tank (not shown). The enlarged time series (Figure 5e) shows the random behavior of the fluctuations, which are superimposed on the low-frequency flow oscillation.

Frequency analysis

The determination of the characteristic macroinstability frequency is essential in order to accurately assess the timescale of

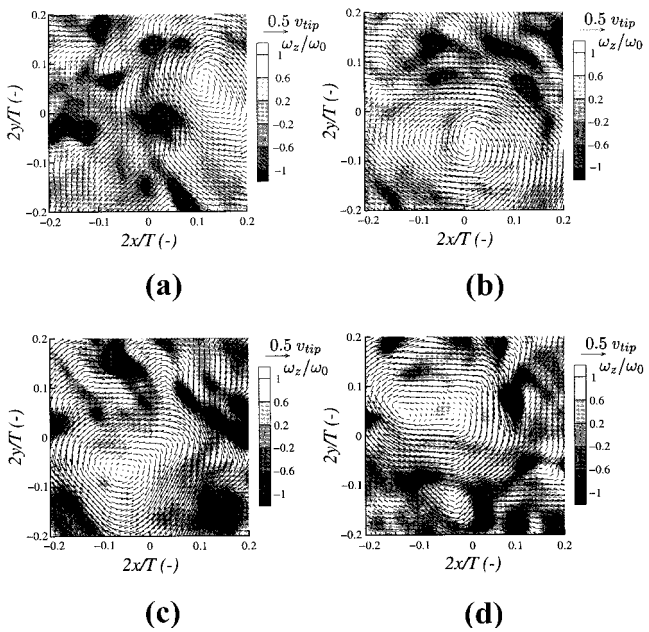

Figure 3. Impressions of the flow field (Case IV) about the tank centerline at four different points in time.

The gray scales represent the axial vorticity component, ω_z, made dimensionless with the impeller angular speed, $\omega_0 = 2\pi N$. (a) Snapshot at the level $z/T = 0.12$. (b) As in (a) after 11 impeller revolutions. (c) As in (a) after 22 impeller revolutions. (d) As in (a) after 33 impeller revolutions.

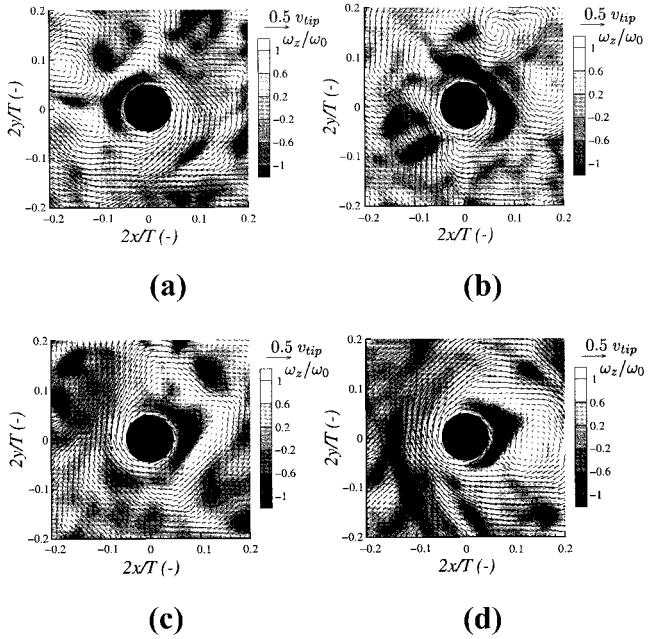

Figure 4. Impressions of the flow field (Case IV) about the tank centerline at four different points in time

The gray scales represent the dimensionless axial vorticity component. The black circle represents the impeller shaft. (a) Snapshot at the level $z/T = 0.88$. (b) As in (a) after 11 impeller revolutions. (c) As in (a) after 22 impeller revolutions. (d) As in (a) after 33 impeller revolutions.

the flow motion. Therefore, the power density spectra of the velocity components were analyzed at all monitoring points. The time series recorded, with a length of 570 impeller revolutions, were first detrended and multiplied with a Hanning window (Oppenheim et al., 1983). Subsequently, the power density spectra were obtained by means of the FFT technique.

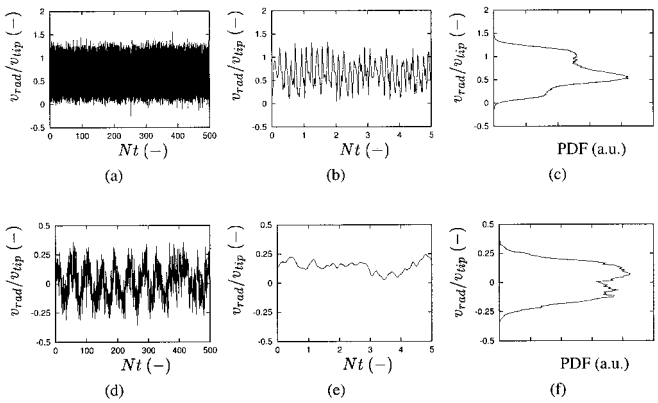

Figure 5. Traces of the simulated radial velocity component (Case IV) at positions $z/T = 0.5$; $2r/T = 0.367$ (a and b) and $z/T = 0.12$; $2r/T = 0$ (d and e).

Please note the different record lengths of 500 (a and d), and 5 (b and e) impeller revolutions, respectively. The PDF's of the time series shown in (a) and (d) are given in (c) and (f), respectively.

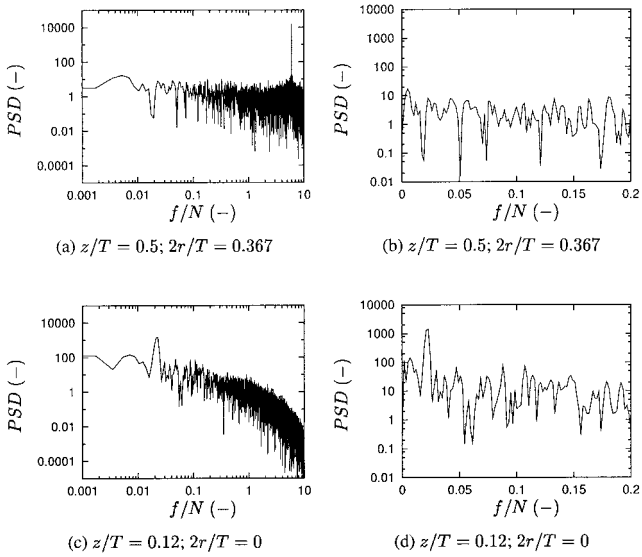

Figure 6. Power Spectral Density functions (Case IV) of the radial velocity component in the impeller outflow region (a and b), and the bulk region (c and d). (a and c) are log-log plots. (b and d) are frequency enlarged lin-log plots.

The frequency resolution of the power density spectra equals $570^{-1}\ N \approx 0.00175N$.

As an illustration, the power density spectra of the presented time-series of the radial velocity component in Figures 5a and 5d are shown in Figure 6. Note that only a selection of frequencies in the power density spectra are presented, the maximum detectable frequency is $0.5f_s = 0.5$ (the Nyquist frequency), which equals $f = 800N$. The spatial resolution of the simulations, however, can not keep up with this high frequency. A more meaningful estimate of the highest frequency that contains flow information is based on (twice) the grid-spacing and typical values of the RMS velocity. If we take $0.4v_{tip}$ for the latter, we get $f = 32N$.

In the impeller outflow region, the turbulent fluctuations are mostly periodic due to the passage of the six impeller blades (see Figure 5a). This is confirmed in the power density spectrum of the radial velocity component, Figure 6a; a clear and distinct peak is observed at $f = 6N$. Furthermore, the power density of this frequency peak is about three to four orders of magnitude larger than the power density of the lower frequencies. No other distinct peaks are observed in the spectra. These observations indicate that a large amount of the kinetic energy (that is, the integral of the area under peak at $f = 6N$) is due to coherent velocity fluctuations caused by the blade passages only.

The time series of the radial velocity component at the monitoring point located in the bulk region ($z/T = 0.12$, $2r/T = 0$) clearly shows a cyclic variation of the mean flow superimposed on the turbulent fluctuations (Figure 5d). This cyclic variation is confirmed in the power density spectrum of the radial velocity component. A clear peak is observed at frequency $f = 0.0228N$, which corresponds to a period of about 44 impeller revolutions. The power density of this peak is more than 10 times larger than that of the other frequencies. More important, the power density of the lower frequencies $f \lessapprox 0.1N$ is significantly higher with respect

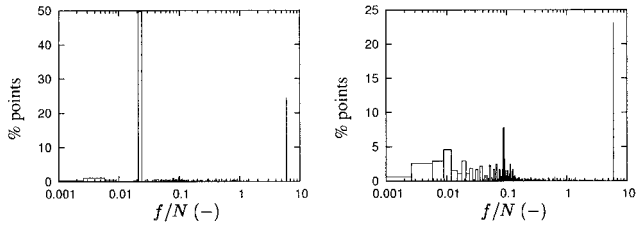

(a) Case IV; Re=30, 000, 180^3-grid (b) Case II; Re=12, 500, 180^3-grid

Figure 7. Histogram of maximum frequency peaks found in the power density spectra of the velocity components.

to that obtained at the monitoring point in the impeller outflow region. Referring to the discussion about the turbulence modeling within the RANS framework in the introduction, this power density spectrum clearly illustrates the absence of a spectral gap between the MI-induced fluctuations, and the random fluctuations (consistent with Nikiforaki et al. (2002)).

The power density spectra were analyzed at all monitoring points, and the results of the principal frequencies (that is, the frequency with the maximum power density) are presented in Figure 7a. These results indicate that around 50% of all monitoring points give the principal frequency at $f = 0.0228N$. Also, a significant amount of monitoring points give the principal frequency at $f = 6N$, which is the blade passage frequency. The characteristic frequency of $f = 0.0228N$ was found in the simulated time series of the axial component as well, albeit at less monitoring points (30%, not shown). This may indicate that the axis of the vortex is essentially oriented in the axial direction.

A similar spectral analysis of the velocity components was performed on the basis of the simulation at $Re = 20{,}000$ (Case III). The results of the spectral analysis indicate, in addition to the distinct blade passage frequency, a clear MI-frequency peak at $f = 0.0255N$. Nikiforaki et al. (2002) observed in a similar Rushton turbine stirred tank with clearance $T/2$, a characteristic frequency of $f = 0.013N - 0.018N$ in the Reynolds number range of $Re = 16{,}000 - 48{,}000$. The frequencies we found are encouraging in the sense that LES proves to be capable of reproducing the precessing vortex phenomenon. The observed deviation from the experimentally found frequencies (which is not that significant in view of the experimental and numerical accuracy) challenges further improvement of the subgrid-scale model and/or the numerical settings.

Effect of Reynolds number and impeller off-bottom clearance

Galletti et al. (2004) confirmed the established linear dependence of the macroinstability frequency by Nikiforaki et al. (2002) of $f \cong = 0.02N$, however, they found that macroinstabilities exhibited a different behavior when considering the laminar, transitional and turbulent Re regions. This lead to different values of f/N. Three regions were defined: Region 1 ($400 < \mathrm{Re} < 6{,}300$), with a single peak at $f = 0.106N$, Region 2 ($6{,}300 < \mathrm{Re} < 13{,}600$), with two peaks at $f = 0.106N$ and $f = 0.015N$, and Region 3 ($13{,}600 < \mathrm{Re} < 54{,}400$) with a single peak at $f = 0.015N$. The latter turbulent frequency peak was in agreement with the findings of Nikiforaki et al. (2002), and to our work. To enhance the confidence in the LES method, a case was defined with Re= 12,500 (that is, Case II). Similar to the histogram of Case IV shown in Figure 7a, a histogram based on the results of Case II is presented in Figure 7b. The turbulent frequency peak is found not that pronounced and clearly defined compared to Case IV at Re= 30,000 ($f \approx 0.012N$). However, another clear peak emerged at $f = 0.092N$. This frequency peak is in good agreement with the experimentally obtained laminar frequency peak $f = 0.106N$, by Galletti et al. (2004).

Galletti et al. (2004) investigated experimentally the effect of the impeller off-bottom clearance on the macroinstability frequency. They observed no significant variation in the macroinstability frequency, and, therefore, the clearance has no pronounced effect on the macroinstability, both for the laminar and turbulent regions. However, flow visualisation results (Yianneskis, 2004) indicated that the instabilities were more pronounced, and more clearly defined with the Rushton turbine located at $C/T = 0.5$. This has been the major reason for us that we set the impeller off-bottom clearance fixed at $C/T = 0.5$.

Pseudo turbulence determination procedure

Velocity fluctuations in a turbulently stirred tank are partly periodic and partly random. The time series presented indicate that in addition to the random turbulent fluctuations, coherent oscillations with a low-frequency are present in stirred tank flow. While in the impeller region such oscillations are directly related to the blade passage frequency, in the bulk flow a precessing vortex motion induces these oscillations. The previous section has shown that the time-scales related to both phenomena differ by more than two orders of magnitude. As a result, the kinetic energy can be divided in a coherent part and a random part. The coherent contribution to the kinetic energy is sometimes presented as pseudo-turbulence (Van 't Riet and Smith, 1975). The kinetic energy in the velocity fluctuations k, is defined as follows

$$k = \tfrac{1}{2}(\overline{u_i^2} - \overline{u}_i^2) = k_{ran} + k_{bpf} + k_{MI} \tag{5}$$

where k_{ran} is the random contribution to the kinetic energy, and k_{bpf} and k_{MI} are the coherent contributions to the kinetic energy related to the blade passage frequency and the precessing vortex, respectively. Note the summation convention over the repeated index i. The (time) averages are over all velocity samples, regardless of the angular position of the impeller.

The coherent part of the kinetic energy related to the blade passage frequency, can easily be removed if angle-resolved average data are available

$$k - k_{bpf} = k_{ran} + k_{MI} = \tfrac{1}{2}(\langle\overline{u_{i\theta}^2}\rangle - \langle\overline{u_{i\theta}}^2\rangle) \tag{6}$$

with $u_{i\theta}$ the i^{th} resolved velocity component sample at the angular position θ. Consequently, the time averages are over the velocity samples at the angular position θ. The notation $< >$ denotes averaging over all angular positions. Each velocity sample v_j at time $t_j = j\delta t$ (or angle $\theta_j = j{\cdot}2\pi\mathrm{N}\delta t$) is ascribed to an angular position with respect to an impeller blade as follows

$$\theta = mod\left(2\pi jN, \frac{\pi}{3}\right) \tag{7}$$

With an angular velocity of $(1{,}600\delta t)^{-1}$, exactly 800 velocity samples cover the angular range $(0 - \pi)$. With Eq. 7, the angular positions within this range are reflected in the range $(0-\frac{2}{3})$, with an angular resolution of $\frac{2}{3}\pi N\delta t$. A velocity time series of 570 impeller revolutions results in a number of 1,140 velocity samples at each angular position, which is sufficient for meaningful flow statistics.

The aforementioned angle averaging practice is straightforward for the extraction of the kinetic energy content related to the blade passage frequency, as this frequency and its phase are fixed and imposed to the flow. The precessing vortex, however, is a flow property, and although the frequency of its precessional motion is well-defined, its motion is not. The vortex certainly precesses in a clock-wise direction as is indicated in Figures 3 and 4, but due to the turbulent behavior of the flow, the vortex position fluctuates about its mean motion. Therefore, the described angle averaging practice can not be applied for determining the kinetic energy in the velocity fluctuations related to the precessing vortex phenomenon.

The kinetic energy content related to the MI can be estimated by means of a filtering procedure. The difficulty is which frequency range and what amount of power contained within this range should be accounted to the MI since (as we discussed above) the MI is not spectrally separated from the rest of the fluctuations. Roussinova et al. (2000) applied a moving average filter to their measured LDA signals with different time window sizes, related to a number of blade passages. We used a low-pass filter, and (as a first approximation) attributed the power content below the cut-off frequency to the coherent velocity fluctuations related to the precessing vortex.

The influence of the filter bandwidth is shown in Figure 8. At the position in the bulk flow, the kinetic energy content of the filtered signal k_f sharply increases at a cut-off frequency close to f_{MI}. This sharp increase is not found in the filtered signal

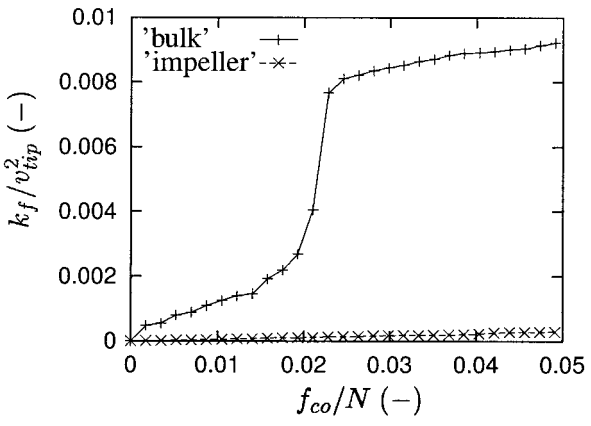

Figure 8. The kinetic energy k_f of the low-pass filtered time series of the radial velocity component (shown in Figures 5a and 5d) as function of the low-pass filter cut-off frequency (f_{co}).

The labels 'bulk' and 'impeller' correspond with positions $z/T = 0.12$; $2r/T = 0$, and $z/T = 0.5$; $2r/T = 0.367$, respectively.

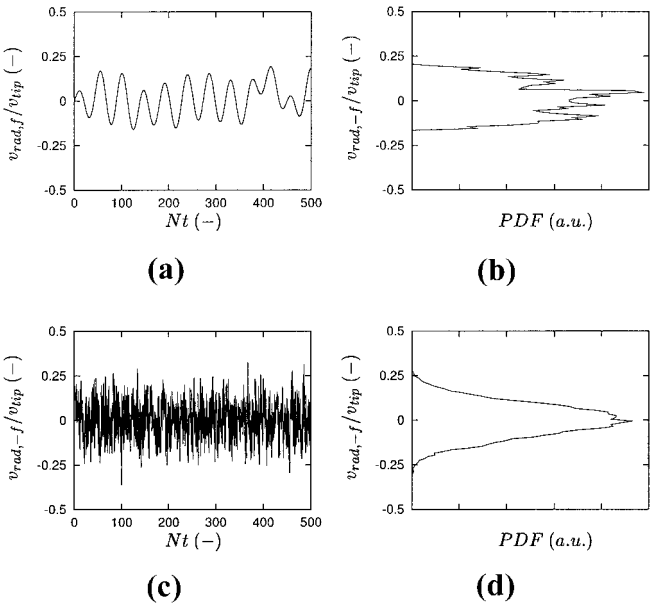

Figure 9. Results of the low-pass filtering procedure on the time series of the radial velocity component shown in Figure 5d.

$v_{rad,f}$ is the filtered radial velocity component, and $v_{rad,-f}$ is the time series of the radial velocity component after removal of the low-frequency content. (a) Time series of the radial velocity component after the low-pass filtering procedure. (b) PDF of the time series shown in (a). (c) Time series of the radial velocity component after removal of the low-frequency content. (d) PDF of the time series shown in (c).

obtained in the impeller outflow region. Moreover, the filtered kinetic energy content in the bulk of the tank is found to be much larger than in the impeller outflow region. Henceforth, the kinetic energy content related to the MI is attributed to the power content in the frequency range: $0 \leq f \leq 0.0228N$. As an illustration of the filtering process, the time series of the radial velocity component shown in Figure 5d is filtered and shown in Figure 9a, with its pdf in 9b. Figure 9c gives the time series without the low-frequency content, and its pdf is shown in Figure 9d. The pdf shows that the velocity fluctuations in the filtered time series are more or less Gaussian distributed. Therefore, it can be concluded that the coherent low-frequency content is almost completely removed from the original time series by the filtering procedure.

Kinetic energy

The kinetic energy in a large eddy simulation is partly resolved and partly unresolved. The kinetic energy residing at the subgrid scales can be estimated based on isotropic, local-equilibrium mixing-length reasoning (Mason and Callen, 1986). A comparison between the grid scale and subgrid scale kinetic energy (instant realization) in a midway baffle plane resulted in the conclusion that the subgrid scale kinetic energy was at least one-order of magnitude less than the grid scale kinetic energy (Derksen, 2003). Therefore, the subgrid scale contribution to the total kinetic energy was neglected, and, in the following results, the total kinetic energy is the resolved total kinetic energy.

The precessing vortex motion has important implications for

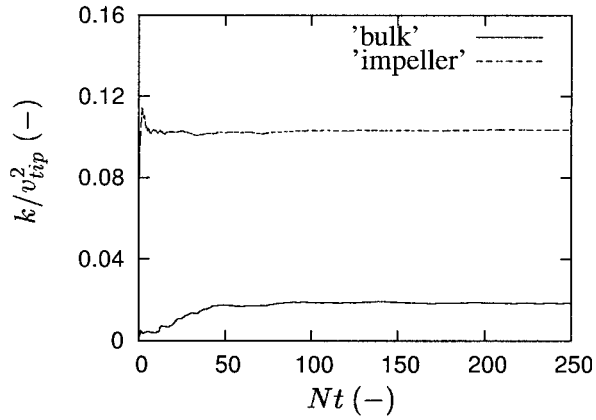

Figure 10. The development of the kinetic energy as function of time series record length (Case IV).

The monitoring points at positions $z/T = 0.12$; $2r/T = 0$, and $z/T = 0.5$; $2r/T = 0.367$ are labeled "bulk" and "impeller", respectively.

the determination of the kinetic energy contained in the velocity fluctuations. For an accurate prediction of the kinetic energy, a couple of precessing vortex periods needs to be captured (see Figure 10). The line labeled "bulk" is obtained from the time series presented in Figure 5d. More than 100 impeller revolutions (that is, roughly two precessing vortex periods) are needed for a more or less constant value of the kinetic energy. In the impeller outflow region the influence of the precessing vortex on the value of the kinetic energy is negligible, which is shown by the line labeled "impeller" in Figure 10. Here, around 10 impeller revolutions are sufficient for an accurate prediction of the kinetic energy.

Four axial profiles of the total kinetic energy are shown in Figure 11. These results are based on record lengths of the

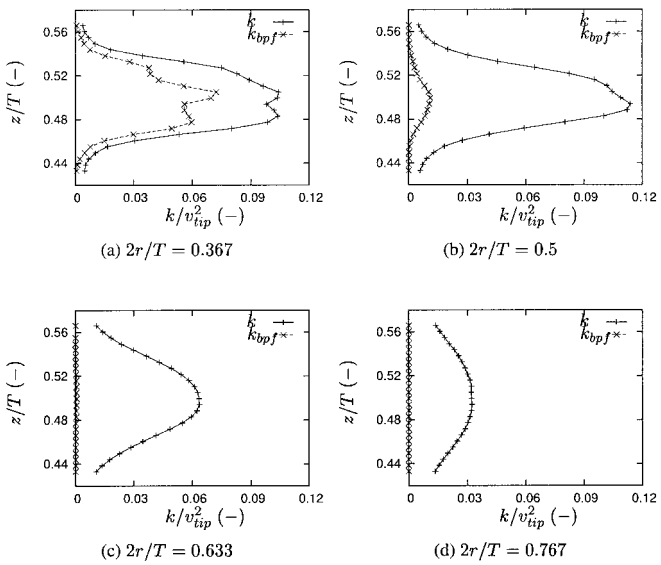

Figure 11. Axial profiles of the kinetic energy at several radial positions (Case IV). A distinction between kinetic energy and kinetic energy related to random velocity fluctuations is made.

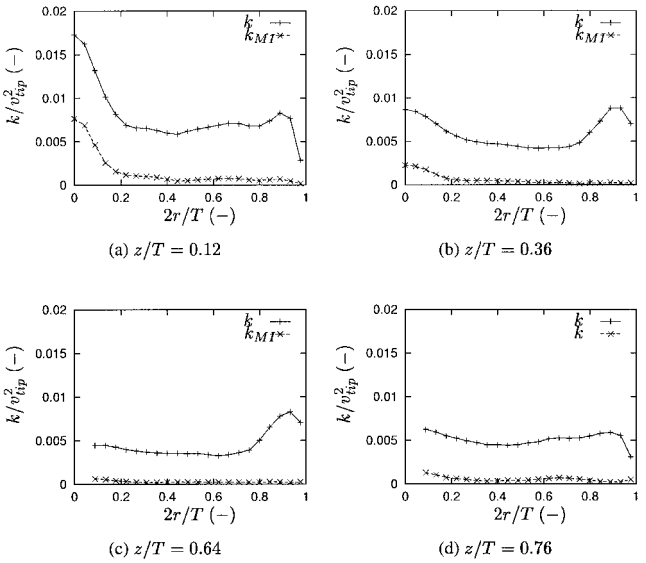

Figure 12. Radial profiles of the kinetic energy at several axial positions (Case IV). A distinction between kinetic energy and MI kinetic energy is made.

velocity components corresponding to 570 impeller revolutions. Close to the impeller tip at $2r/T = 0.367$, a large amount of the kinetic energy is found to be related to the coherent blade passage frequency. This blade passage contribution to the kinetic energy decreases rapidly as the distance from the impeller tip becomes larger; from $2r/T = 0.633$ radially outward, this contribution becomes negligible. The contribution of the precessing vortex to the kinetic energy was found negligible in the impeller outflow region (less than 1% of the total kinetic energy).

Figure 12 shows four typical radial profiles of the total kinetic energy over record lengths of 570 impeller revolutions. This number of revolutions is sufficient for a constant value of the kinetic energy. Next to the radial profiles of the kinetic energy, the radial profiles of the kinetic energy of the macroinstability related velocity fluctuations are shown. The coherent blade passage contribution to the kinetic energy was found negligible (less than 0.1% of the total kinetic energy) at all monitoring points located on the horizontal lines. The radial profiles of the kinetic energy are approximately flat in the region $0.2 < 2r=T < 0.8$. Increased k-levels are observed along the tank wall as a result of the impeller outflow. Also around the tank centerline, increased k levels are found. This effect is found more pronounced in the domain below the impeller. About the tank centerline, there is a significant contribution to the kinetic energy due to the passage of the precessing vortex, being 44% of the total kinetic energy at $z/T = 0.12$, 26% at $z/T = 0.36$, 14% at $z/T = 0.64$ and 21% at $z/T = 0.76$. These percentages illustrate in the first place that the MI is more pronounced in the absence of the impeller shaft. In the second place, the contribution of the MI to the kinetic energy is most significant in the top and bottom parts of the tank at $2r/T < 0.2$. At radial positions larger than about $2r/T = 0.2$, the MI effect on the turbulence levels is less than 10%. These latter observations imply that the precessing vortex moves in the area $2r/T < 0.2$, which was already suggested by Figures 3 and 4.

Grid size effects

The results presented were based on simulations performed on the 180^3-grid. It is interesting to study the effect the grid size may have on the (spatial) resolution of the precessing vortex motion. Therefore, the stirred tank flow at Re= 20,000 has been simulated on two grid sizes: a coarser 120^3-grid and the standard 180^3-grid. The frequencies containing the maximum power density were captured and put into a histogram (see Figure 13). The histograms show that the blade passage frequency is accurately found at both grid sizes. A broad range of low frequencies (that is, $f < N$) is found at the 120^3-grid, but a clear dominant peak due to the MI phenomenon is not observed. Contrary to this, the histogram for the 180^3-grid does show a clear dominant frequency peak at $f = 0.0255N$.

Next, a second flow simulation at Re=30,000 has been performed on a finer grid (that is, 240^3 grid nodes, Case V). Because of the higher computational demand, 150 rather than 570 impeller revolutions were simulated. This number of revolutions is not enough to accurately determine the characteristic frequency, and the consequent MI impact on the fluctuation levels. Nevertheless, the time series of the velocity components indicated the existence of the precessing vortex motion. As an illustration, the time series of the radial velocity component is shown for two typical positions; one in the bottom part of the tank and one in the top part of the tank (in Figure 14). They clearly show consistent behavior compared to the results presented for Case IV in terms of the principal frequency, phase difference between upper and lower vortices, and the strength of the mean flow variation. The time-series confirm the precessing vortex motion, with a characteristic frequency of $f = 0.02N - 0.025N$ (based on two periods). As grid refining did not lead to a better agreement between the experimental and numerical result of the characteristic frequency, the conclusion for the time being is that improvement of the subgrid-scale model may lead to a better correspondence. In view of the simulations performed, a grid of 180^3 nodes is necessary and sufficient to resolve the precessing vortex motion at the Reynolds numbers investigated.

From Figures 3 and 4, the size of the precessing vortex can be estimated. With a view to the discussion earlier, it appears that on the 180^3-grid about 10–20 grid cells are required to accurately resolve the precessing vortex. This leads to a diameter of the vortex of about $T/18$–$T/9$.

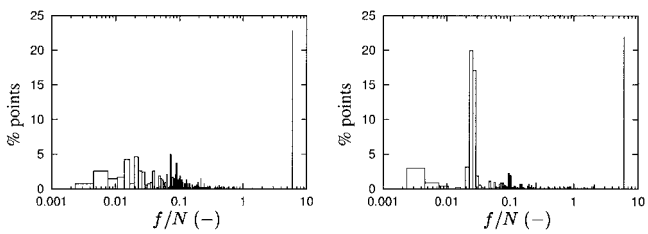

(a) Case I; Re=20,000, 120^3-grid (b) Case II; Re=20,000, 180^3-grid

Figure 13. Histograms of maximum frequency peaks found in the power density spectra of the velocity components.

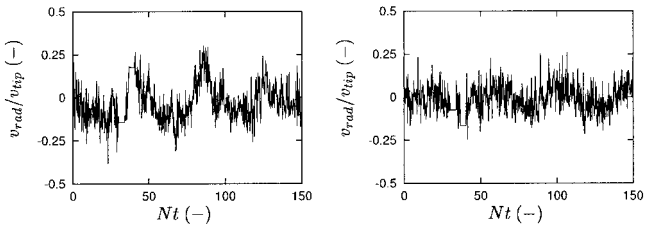

(a) $z/T = 0.12$; $2r/T = 0.1$ (b) $z/T = 0.88$; $2r/T = 0.1$

Figure 14. Traces of the radial velocity component at two typical positions in the bulk of the tank.

The two horizontal line segments around $Nt = 40$ are due to processing errors during the simulation. This simulation was performed on the fine 240^3-grid at Re=30,000 (Case IV).

Conclusions

In this article, we have investigated the precessing vortex phenomenon (that is, a macroinstability) numerically in a Rushton turbine stirred tank by means of large eddy simulations. Such an in vestigation is worthwhile for the determination of the integral timescale of the flow motion, and the significance of the precessing vortex with respect to the fluctuation levels and the flow patterns.

The presence of precessing vortices has important implications for numerical simulations of stirred tank flows. The vortex motion is a transient phenomenon, which cannot be captured in a quasi steady-state simulation, and reduction of the computational domain because of symmetry properties of the geometry is not possible. We have performed large eddy simulations instead of RANS simulations, because, within the LES methodology, the scales of interest are directly resolved, and there is a clear dinstinction between the resolved and unresolved scales. Furthermore, we avoided the interface models commonly applied for the calculation of stirred tank flows in commercial codes, since it is unclear how significant the (spatial) resolution of the precessing vortex motion is affected by the location of the interface between the rotating and stationary meshes, and by the interface model itself.

The sequences of snapshots of the flowfield in a horizontal plane below and above the impeller showed a vortical structure moving around the tank centerline in the same direction as the impeller. The vortex below the impeller was found more pronounced in strength and size compared to the vortex above the impeller, and both vortices move with a mutual phase difference. The presented time series of the velocity components reveal, besides the random turbulent fluctuations, two types of coherent fluctuations with timescales separated by more than two-orders of magnitude. The fluctuations in the impeller outflow region are dominated by the passage of the impeller blades, whereas fluctuation levels close to the tank centerline are dominated by the low-frequency motion of a vortical structure.

A frequency analysis provided the characteristic frequencies of $f = 0.0255$N and $f = 0.0228$N at flow Reynolds numbers of 20,000 and 30,000, respectively. The determined values of the characteristic MI frequency are in good agreement with reported (turbulent) frequencies found experimentally in a similar flow geometry. At a Reynolds number of 12,500, a second frequency peak at $f = 0.092N$ was observed, which is consis-

tent with the experimentally observed frequency, the so-called laminar frequency, in the literature.

Meaningful flow statistics can only be extracted if the flow is calculated in a time span covering several integral timescales. In the impeller outflow region with $2r/T \leq 0.63$, the flow is dominated by the passage of the impeller blades. A time span covering several blade passage periods is sufficient here. In the bulk flow region with $2r/T \leq 0.2$, the flow is dominated by the low-frequency precessing vortex, and at least 100 impeller revolutions need to be captured for an accurate prediction of the kinetic energy contained in the velocity fluctuations. By means of a low-pass filtering procedure, it has been observed that, in the top and bottom parts of the tank at $2r/T \leq$, 0.2 a significant amount (up to 44%) of the kinetic energy is related to the precessing vortex.

The stirred tank flow has been simulated using three different lattice node densities. The main conclusion is that a grid size of 180^3 lattice nodes is necessary and sufficient for resolving the vortex motion at the Reynolds numbers investigated.

LES has proven its significance in the prediction of the precessing vortices present in a stirred tank flow. The detailed results gave insight in the structure and characteristic frequency of the vortices, and drew attention to the precessing vortex as a point for improvement in the existing modeling techniques. Furthermore, the results form a promising perspective for the application of the LES methodology in future studies considering the significance of the precessing vortex in multiphase mixing processes.

Acknowledgments

The authors acknowledge financial support for the "OPTIMUM" project provided by the Commission of the European Union under the program "Promoting Competitive and Sustainable Growth", Contract G1RD-CT-2000-00263. Prof M. Yianneskis from King's College London, and Dr. B. Genenger from the University of Erlangen are acknowledged for their input to this work.

Notation

c_s = Smagorinsky constant
D = impeller diameter, m f frequency, 1/s
f_{co} = low-pass filter cut-off frequency, 1/s
k = kinetic energy in the velocity fluctuations, m^2/s^2
k_{bpf} = kinetic energy in the velocity fluctuations related to blade passage frequency, m^2/s^2
k_f = kinetic energy in the velocity fluctuations after low-pass filtering, m^2/s^2
k_{MI} = kinetic energy in the velocity fluctuations related to the macro-instability, m^2/s^2
k_{ran} = kinetic energy in the velocity fluctuations related to turbulence, m^2/s^2
N = impeller speed of revolution, 1/s
r = radial coordinate, m
S = resolved deformation rate, 1/s
t = tank diameter, m
u_i = velocity component i, m/s
$u_{i\theta}$ = velocity component i linked to an angular position, m/s
u_i' = fluctuating velocity component i, m/s
v_j = velocity sample, m/s
v_{rad} = radial velocity component, m/s
$v_{rad,f}$ = radial velocity component after low-pass filtering, m/s
$v_{rad,-f}$ = radial velocity component after removal of low-frequency content, m/s
v_{tip} = impeller tip speed, m/s
x,y = Carthesian coordinates, m
y^+ = distance from wall in viscous wall units
z = axial coordinate, m
Δ = lattice spacing, m
θ = angle, rad
θ_j = discrete angle, rad
λ_{mix} = mixing length, m
ν = kinematic viscosity, m^2/s
ν_e = Smagorinsky eddy viscosity, m^2/s
τ = wall-clock time needed for calculating a single impeller revolution, s
ω_z = axial vorticity component, rad/s
ω_{θ} = impeller angular speed of revolution, rad/s

Literature Cited

CFX-5. User Manual, Solver and Solver Manager, ANSYS, Inc., Canonsburg, PA (2002).
Chen, S., and G. D. Doolen, "Lattice-Boltzmann Method for Fluid Flows," *Ann. Rev. Fluid Mech*., **30**, 329 (1998).
Derksen, J. J., "Numerical Simulation of Solids Suspension in a Stirred Tank," *AIChE J*., **49**, 209 (2003).
Derksen, J. J., S. Doelman, and H. E. A. Van den Akker, "Three-Dimensional LDA Measurements in the Impeller Region of a Turbulently Stirred Tank," *Exp. Fluids*, **27**, 522 (1999).
Derksen, J. J., H. E. A. Van den Akker, "Large Eddy Simulations on the Flow Driven by a Rushton Turbine," *AIChE J*., **45**, 209 (1999).
Eggels, J. G. M., "Direct and Large-Eddy Simulations of Turbulent Fluid Flow Using the Lattice-Boltzmann Scheme," *Int. J. Heat. Fluid. Flow*, **17**, 307 (1996).
Galletti, C., K. C. Lee, A. Paglianti, and M. Yianneskis, "Reynolds Number and Impeller Diameter Effects on Instabilities in Stirred Vessels," *AIChE J*., **50**, 2063 (2004).
Haam, S, R. S. Brodkey, J. B. Fasano, "Local Heat Transfer in a Mixing Vessel Using Heat Flux Sensors," *Ind. Eng. Chem. Res*., **31**, 1384 (1992).
Hartmann, H., J. J. Derksen, C. Montavon, J. Pearson, I. S. Hamill, and H. E. A. Van den Akker, "Assessment of Large Eddy and RANS Stirred Tank Simulations by Means of LDA," *Chem. Eng. Sci.*, **59**, 2419 (2004).
Hasal, P., J. L. Montes, H. C. Boisson, and I. Fort, "Macro-Instabilities of Velocity Field in Stirred Vessel: Detection and Analysis," *Chem. Eng. Sci*., **55**, 391 (2000).
Holmes, D. B, R. M.Voncken, and J. A. Dekker, "Fluid Flow in Turbine Stirred, Baffled Tanks I: Circulation Time," *Chem. Eng. Sci*., **19**, 201 (1964).
Houcine, I, E. Plasari, R. David, and J. Villermaux, "Feedstream Jet Intermittency phenomena in Continuous Stirred Tank Reactor," *Chem. Eng. J*., **72**, 19 (1999).
Luo, H, and H. F. Svendsen, "Theoretical Model for Drop and Bubble Breakup in Turbulent Dispersions," *AIChE J*., **42**, 1225 (1996).
Mason, P. J., and N. S. Callen, "On the Magnitude of the Subgrid-Scale Eddy Coefficient in Large-Eddy Simulations of Turbulent Channel Flow," *J. Fluid Mech*., **162**, 439 (1986).
Myers, K. J., R. W. Ward, and A. Bakker, "A Digital Particle Image Velocimetry Investigation of Flow Field Instabilities of Axial-Flow Impellers," *ASME J., Fluids Eng.,* **119**, 623 (1997).
Nikiforaki, L, G. Montante, K. C. Lee, and M. Yianneskis, "On the origin, frequency and Magnitude of Macro-Instabilities of the Flows in Stirred Vessels," *Chem Eng Sci*., **58**, 2937 (2002)
Oppenheim, A. V., A. S.Willsky, and I. T. Young, *Signals and Systems*, Prentice Hall, Englewood Cliffs, NJ (1983).
Piomelli, U, P. Moin, and J. H. Ferziger, "Model Consistency in Large Eddy Simulation of Turbulent Channel Flows," *Phys. Fluids*, **31**, 1884 (1988).
Roussinova, V, Grgic B, S. M. Kresta, "Study of Macro-Instabilities in Stirred Tanks Using a Velocity Decomposition Technique," *Trans. IChemE*., **78A**, 1040 (2000)
Roussinova, V, S. M. Kresta, and R. Weetman, "Low Frequency Macro-instabilities in a Stirred Tank: Scale-Up and Prediction Based on Large Eddy Simulations," *Chem. Eng. Sci*., **58**, 2297 (2003).
Rushton, J. H., E. W. Costich, and H. J. Everett, "Power Characteristics of Mixing Impeller I and II," *Chem. Eng. Prog*., **46**, 395 (1950).
Schäfer, M, M. Yianneskis, P. Wächter, and F. Durst, "Trailing Vortices Around a 45° Pitched-Blade Impeller," *AIChE J*., **44**, 1233 (1998).
Smagorinsky, J., "General Circulation Experiments with the Primitive Equations: 1. The Basic Experiment," *Mon. Weather Rev*., **91**, 99 (1963).

Somers, J A., "Direct Simulations of Fluid Flow with Cellular Automata and the Lattice-Boltzmann Equation," *Appl. Sci. Res*., **51,** 127 (1993).
Tsouris, C., and L. L. Tavlarides, "Breakage and Coalescence Models for Drops in Turbulent Dispersions," *AIChE J.*, **40**, 395 (1994).
Van Driest, E. R., "On Turbulent Flow Near a Wall," *J. Aero. Sci*., **23**:1007 (1956).
Van 't Riet, K., and J. M. Smith, "The Trailing Vortex System Produced by Rushton Turbine Agitators," *Chem. Eng. Sci.*, **30**, 1093 (1975).
Van Vliet E., J. J Derksen, and H. E. A. Van Den Akker, "Modelling of Parallel Competitive Reactions in Isotropic Homogeneous Turbulence using a Filtered Density Approach for Large Eddy Simulations," *Proc. of the ASME-PVP "3rd Int. Symp. on Computational Technologies for Fluid/Thermal/Chemical Systems with Industrial Applications,"* The American Society of Mechanical Engineers, New York, ASME-PVP-Vol. 424-2, 35 (2001).
Wilcox, D. C. *Turbulence Modelling for CFD*, DCW Industries La Canada, CA (1993).
Yianneskis M., Private Communication (2004).
Yianneskis, M., Z. Popiolek, and J. H. Whitelaw. "An Experimental Study of the Steady and Unsteady Flow Characteristics of Stirred Reactors," *J. Fluid Mech*., **175**, 537 (1987).

Manuscript received July 15, 2003, and revision received Feb. 5, 2004.